Contribution of the location and spatial pattern of initial error to uncertainties in El Niño predictions

Yanshan Yu,[1] Mu Mu,[1] Wansuo Duan,[2] and Tingting Gong[1]

Received 15 November 2011; revised 4 May 2012; accepted 4 May 2012; published 26 June 2012.

[1] With the Zebiak-Cane model, the contribution of the location and spatial pattern of initial error in sea surface temperature anomalies (SSTA) to uncertainty in El Niño predictions is investigated using an approach based on conditional nonlinear optimal perturbation (CNOP), which seeks to find the initial error (i.e., the CNOP error) that satisfies a given constraint and that causes the largest prediction error at the prediction time. The computed CNOP error of SSTA has a dipole pattern in the equatorial central and eastern Pacific. The initial error from the equatorial central and eastern Pacific tends to grow more significantly than those from other locations. Because of the contribution of annual mean states the location of the initial error plays an important role in the error evolution; e.g., the shallow annual mean thermocline in the eastern Pacific favors feedback between the thermocline and sea surface temperature. Meanwhile, the specific dipole structure of the initial error is also crucial for optimal error growth. Even with the same magnitude as the CNOP error, random initial error in the equatorial central and eastern Pacific does not evolve significantly over time. Initial errors of SSTA with a similar spatial pattern to the CNOP error (i.e., the dipole pattern of SSTA error) give rise to larger prediction errors than those without similar spatial pattern do. Consequently, the magnitude of the prediction error at the prediction time depends on the combined effects of the location and spatial pattern of the initial error. If additional observation instruments are deployed to observe sea surface temperature with limited coverage, they should preferentially be deployed in the equatorial central and eastern Pacific.

Citation: Yu, Y., M. Mu, W. Duan, and T. Gong (2012), Contribution of the location and spatial pattern of initial error to uncertainties in El Niño predictions, *J. Geophys. Res.*, *117*, C06018, doi:10.1029/2011JC007758.

1. Introduction

[2] Significant progress has been made in ENSO theories and predictions in recent decades [*Wang and Picaut*, 2004], but there remains considerable uncertainty in realistic ENSO predictions [*Jin et al.*, 2008; *Luo et al.*, 2008], possibly due to the uncertainty in initial conditions and model parameters, the inherent nonlinear feature of ENSO, the atmospheric noise and other high-frequency variations [*Jin et al.*, 1994; *Kleeman and Moore*, 1997; *Chen et al.*, 2004; *Moore et al.*, 2006; *Gebbie et al.*, 2007; *Chen and Cane*, 2008; *Tang et al.*, 2008]. The predictability of ENSO in relation to the initial error has attracted much attention, resulting in various approaches such as the linear singular vector (LSV) [*Moore and Kleeman*, 1996; *Chen et al.*, 1997; *Xue et al.*, 1997a, 1997b; *Tang et al.*, 2006; *Zhou et al.*, 2008; *Cheng et al.*, 2010a, 2010b], bred vector [*Cai et al.*, 2003; *Tang and Deng*, 2011] and conditional nonlinear optimal perturbation (CNOP) [*Mu and Duan*, 2003; *Mu et al.*, 2003], which is an extension of a singular vector in the nonlinear regime.

[3] The application of CNOP, in the context of the Zebiak–Cane model [*Zebiak and Cane*, 1987] (hereinafter referred to as the ZC model), has shown that under the constraint of the magnitude measured by the L2 norm, a special kind of initial error (referred to as the CNOP error) with two components (sea surface temperature anomalies (SSTA) and thermocline depth anomalies) generates the largest prediction error; whereas some other initial errors with the same magnitude as the CNOP error give rise to negligible errors [*Mu et al.*, 2007]. *Yu et al.* [2009] investigated the characteristics of the CNOP errors and identified two types of errors, with nearly opposite signs and similar spatial patterns, which could cause significant prediction errors. Error type-1 possesses an SSTA dipole pattern with negative anomalies in the equatorial central Pacific and positive anomalies in the equatorial eastern Pacific, plus positive thermocline depth anomalies in the entire equatorial Pacific; type-2 shows nearly opposite sign to type-1. The dipole pattern of initial error of SSTA, which tends to cause a significant prediction error, has also been identified by *Duan and Wei* [2012] with a coupled general circulation

[1]Key Laboratory of Ocean Circulation and Wave Studies, Institute of Oceanology, Chinese Academy of Sciences, Qingdao, China.
[2]LASG, Institute of Atmospheric Physics, Chinese Academy of Sciences, Beijing, China.

Corresponding author: T. Gong, Key Laboratory of Ocean Circulation and Wave Studies, Institute of Oceanology, Chinese Academy of Sciences, Qingdao 266071, China. (ttg.zxb@gmail.com)

0148-0227/12/2011JC007758

model and by *Duan et al.* [2009] with other statistical methods. *Yu et al.* [2009] pointed out although both the CNOP error and LSV error of the ZC model with the same magnitude possess a SSTA dipole pattern, the CNOP error covers a broader area and causes an obviously larger prediction error than LSV error does in the context of the nonlinear model [*Yu et al.*, 2009, Figure 6]. A localized region of the SSTA component of CNOP errors with large values, which always arises in the equatorial central and eastern Pacific, is likely to help us capture the sensitive area of ENSO predictions, thereby guiding efforts to decrease the initial analysis error in this area and ultimately improve the accuracy of ENSO predictions. Although these previous studies mentioned the location of large values of the initial error that tends to trigger a large prediction error, might be a sensitive area for ENSO prediction, they have not defined a sensitive area or compared the sensitive area with other areas in terms of their effects on prediction errors. Furthermore, it is unknown that if decreasing initial error in sensitive area will indeed provide more benefit than other areas, which will be addressed in this study using initial conditions from operational ENSO forecast.

[4] The accuracy of SST is far from perfect though current generation of infrared and passive microwave satellite provides highly complementary information enabling significant advancement in our ability to monitor SST [*Castro et al.*, 2008]. The accuracy of infrared data is about 0.3–0.4°C RMS [*Kearns et al.*, 2000; *Harris and Saunders*, 1996], but the retrievals can be completely obscured by clouds; the microwave data provide coverage through nonprecipitating clouds but have coarser spatial resolution (∼50 km) and generally poorer accuracy (0.5–0.6°C RMS [*Gentemann et al.*, 2004]). In addition, the analysis errors of SSTA along the equator possess a standard deviation of 0.2°C [*Kaplan et al.*, 1998], larger than the maximum of CNOP error in all the grids 0.08°C [*Yu et al.* 2009, Figure 2]. It means that a CNOP error might exist in the analysis error of SSTA, and could trigger a non-negligible prediction error. Therefore, considering the initial error of SSTA and trying to improve the accuracy of SSTA in a sensitive area is of practical use, and could be considered as a preliminary study of targeted observation in ENSO prediction with CNOP method.

[5] In the past decade, the use of targeted observations to improve numerical forecasts of high-impact weather events has been examined in a series of field programs (see *Langland* [2005] for an overview of targeting programs and relevant references). Given the high cost of observations over ocean, a focus on a localized sensitive area may represent an economical and efficient strategy in terms of targeted observations with the aim of improving prediction skill of ENSO. *Morss and Battisti* [2004a, 2004b] suggested that for forecasts longer than a few months, the most important area for observations is the eastern equatorial Pacific, south of the equator; a secondary region of importance is the western equatorial Pacific. These areas correspond to those where the LSV of their model has large amplitude, and also show some similarities to the locations for CNOP errors in current study (Note that the initial errors from the thermocline depth are not considered here because of the relatively zonally spread and uniform structure of its CNOP in the whole equatorial region, as well as its independence of the SSTA error). For the obtained CNOP errors, there raises several interesting questions. For instance, how much prediction error can be caused by initial error from a non-sensitive area? Whether the maximum prediction error caused by initial error from a non-sensitive area is smaller than that caused by initial error from a sensitive area? Could initial errors existing in the sensitive area but without a dipole pattern induce a non-negligible prediction error? We aim to address these questions by performing a series of experiments with the ZC model. Results of this study demonstrate that both the location and the spatial pattern of the initial errors account for large prediction errors. Thereafter, we also evaluate the improvement of forecast skill by eliminating initial error in the sensitive area identified by CNOP method.

[6] The remainder of this paper is organized as follows. Section 2 describes the design of prediction experiments for model El Niño events, and computes the CNOP error and its evolution for each experiment. Section 3 calculates the individual CNOP errors in six sub-areas, including a defined sensitive area, and shows the contribution of the location of the initial error to uncertainty in El Niño predictions. Section 4 tests the contribution of the spatial pattern of initial errors to the prediction uncertainties by estimating the prediction errors caused by initial random errors and other initial errors with certain spatial patterns superimposed on the predetermined sensitive area. Section 5 examines the effect of targeted observations in terms of improving forecast skill, based on a set of ideal numerical experiments. Finally, Section 6 provides a discussion and a summary for the main results.

2. Conditional Nonlinear Optimal Perturbation

[7] The present numerical experiments employ the ZC model, which is a nonlinear anomaly model of intermediate complexity that describes anomalies about a specified seasonally varying background, avoiding the "climate drift" problem [*Zebiak and Cane*, 1987]. The atmosphere model and the prognostic equation of SSTA are run at a horizontal resolution of $5.625^\circ \times 2.0^\circ$. The ocean model is a grid point model with a horizontal resolution of $2.0^\circ \times 0.5^\circ$.

[8] Integrating the ZC model for 1000 years, we obtain a time series of SSTA, as well as many El Niño events that tend to have a 4-yr period and phase-lock to the end of the calendar year. Eight El Niño events with various intensities and onset times were selected for the numerical experiments. Figure 1 shows time-dependent Niño-3 indices for these eight El Niño events. Note that the selected reference-state El Niño events are considered as "true" states and that our research is based on the assumption of a perfect model. For each El Niño event, we make predictions for 1 year (i.e., a lead time of 1 year) with different 12 start months by superimposing initial errors on the "true" state at different start months. The initial errors are described in details below. We use Year (0) to denote the year when El Niño attains a peak value, and Year (−1) to signify the year before Year (0). In the numerical experiments, El Niño predictions are made with starting months from July (−1) (i.e., July in Year (−1)) to June (0). Because the duration of each prediction is 1 year, error evolution occurs mainly during the growth phase of El Niño events. We focus on the growth-phase predictions,

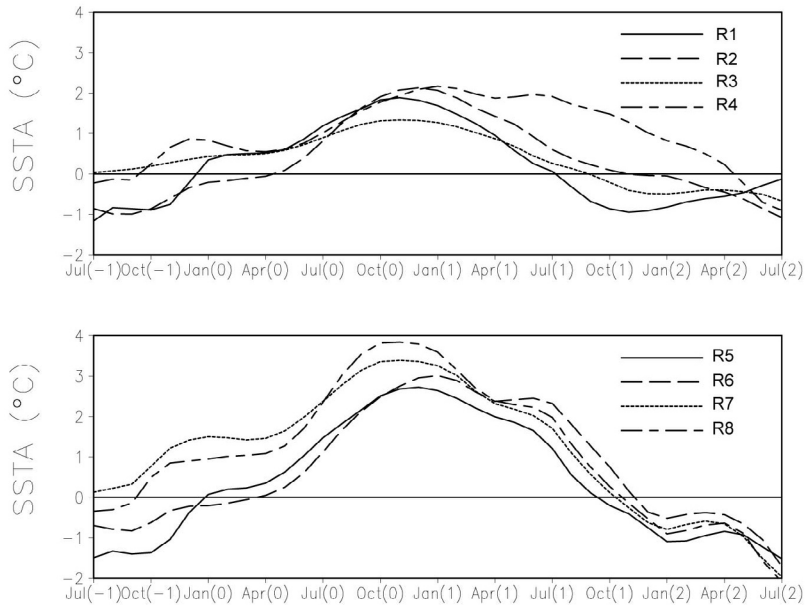

Figure 1. Time-dependent Niño-3 indices of eight El Niño reference states, denoted by Ri (i = 1, 2, …, 8). Start months of predictions for these El Niño events range from July (−1) to June (0).

which could provide the most important information (e.g., the onset times and strengths of the El Niño events).

[9] For each prediction experiment, we seek the initial error (i.e., CNOP error) that causes the largest departure from the "true" state at the prediction time, using the CNOP method. Assuming that initial errors exist only in SSTA, the computed CNOP error consists of only one component: SSTA. To obtain the CNOP error, a cost function is constructed to measure the evolution of the initial error of SSTA. The CNOP error, denoted by $\vec{T}'_{0\delta}$, is obtained by solving the following nonlinear optimization:

$$J(\vec{T}'_{0\delta}) = \max_{\|\vec{T}'_0\|_2 \le \delta} \|\vec{T}'(\tau)\|_2, \tag{1}$$

where $\vec{T}'_0$ is the initial error of the SSTA superimposed on the initial state of a predetermined reference state El Niño event. $\|\vec{T}'_0\|_2 \le \delta$ is the constraint condition defined by a prescribed positive real number δ and the norm $\|\vec{T}'_0\|_2 = \sqrt{\sum_{i,j} T'^2_{0i,j}}$, where $T'_{0i,j}$ represents the initial error of the SSTA at different grid points and (i, j) is the interior grid point in the domain of the tropical Pacific (135°E–90°W at an interval of 5.625°; 17°S–17°N at an interval of 2°). The cost function is the evolution of the initial error at time τ, measured by $\|\vec{T}'(\tau)\|_2 = \sqrt{\sum_{i,j} T'_{i,j}(\tau)^2}$. $\vec{T}'(\tau)$ represents the prediction error of SSTA at time τ, obtained by subtracting the SSTA of the reference state from the predicted SSTA at prediction time τ.

[10] The initial times are the predetermined start months of the El Niño prediction and the time interval is 12 months (i.e., τ = 12 months, corresponding to a lead time of 12 months for El Niño predictions). The constraint bound δ related to the CNOP error was predetermined experimentally to be 1.2, indicating that the errors of SSTA measured by the chosen norm do not exceed 1.2°C. We chose other constraint bounds to calculate the corresponding CNOP errors. The results show that the spatial patterns of optimized CNOP errors are similar, and that differences exist mainly in magnitude, which do not influence the conclusions of this study. As a result, CNOP errors related to other constraint bounds are not presented.

[11] To solve the optimization problem (equation (1)), we used the solver Spectral Projected Gradient 2 (SPG2) [*Birgin et al.*, 2000] to minimize the negativity of the cost function (for details, see *Yu et al.* [2009]). Consequently, a total of 96 CNOP errors are obtained from various combinations of 12 start months and 8 El Niño events. These CNOP errors represent the initial errors of SSTA under a constraint, which caused the largest prediction errors in the 96 prediction experiments. The CNOP errors have a dipole pattern in the tropical Pacific, and can be classified into two categories according to the sign of the resultant prediction error of the Niño-3 index at the prediction time. All CNOP errors that induce positive prediction errors of the Niño-3 index at prediction time are composited as type-1 CNOP error; the other CNOP errors are composited as type-2 CNOP error. The composite CNOP errors are scaled to have equivalent magnitudes to δ. Figure 2 shows these two composite CNOP errors. Type-1 CNOP error comprises negative errors of SSTA in the equatorial central Pacific and positive errors in the equatorial eastern Pacific, resulting in a positive prediction error of the Niño-3 index, while type-2 CNOP error has a sign almost opposite to the former, causing a negative prediction error of the Niño-3 index. For both composite CNOP errors, large SSTA errors occur mainly in the equatorial central and eastern Pacific.

[12] CNOP is the initial perturbation whose nonlinear evolution attains the maximal value of the cost function. Mathematically, it is the global maximum of the objective function in the phase space. In some cases, there exists local maximum of the objective function. And the corresponding initial perturbations are referred to local CNOP. The local

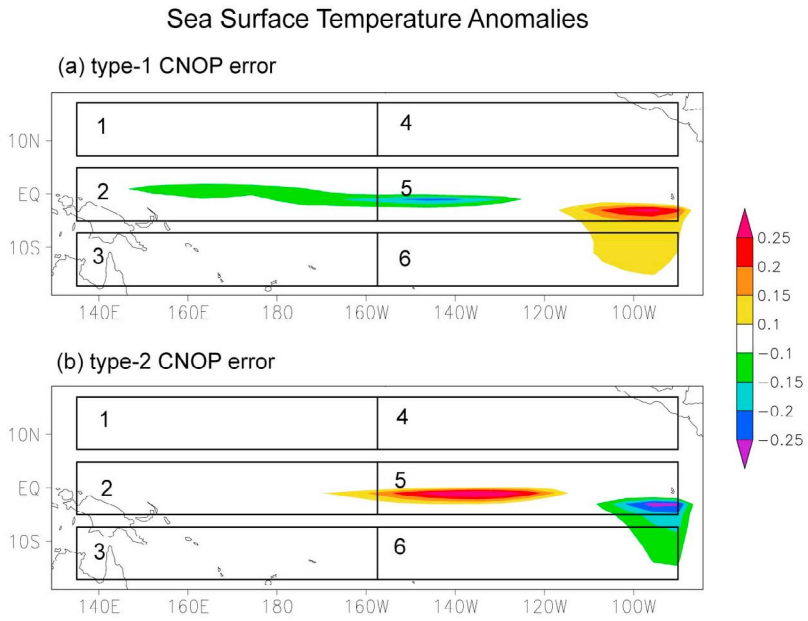

Figure 2. (a, b) Two types of CNOP error shown in six rectangular domains denoted by Domain i (i = 1, …, 6). Large values of both types of CNOP error occur mainly in Domain 5.

CNOP error for a given optimization experiment, which causes the second-largest prediction error, has a spatial pattern similar to that of the CNOP error, but with the opposite sign. Note that the local CNOP error and CNOP error for a given optimization experiment are both related to one particular El Niño event and one particular start month, but that two types of CNOP errors in Figure 2 are composited from many CNOP errors obtained from various combinations of 8 El Niño events and 12 start months. Meanwhile, the CNOP also possesses clear physical meanings [*Duan and Mu*, 2009]. Apart from acting as an initial error that has the largest negative effect on the prediction result at the prediction time, CNOP can also be used to be superimposed on the climatological basic state acts as the initial anomaly mode that is most likely to evolve into an El Nino event and represents the optimal precursor of El Nino [*Duan et al.*, 2004; *Duan and Mu*, 2006; *Duan et al.*, 2008]. In sensitivity analysis studies, CNOP may represent the most unstable mode [*Mu et al.*, 2004; *Sun et al.*, 2005; *Wu and Mu*, 2009; *Terwisscha van Scheltinga and Dijkstra*, 2008].

[13] To further investigate the evolution of the CNOP error, Figure 3 shows snapshots of the prediction errors of SSTA, zonal wind anomalies, and thermocline depth anomalies with lead times of 3, 6, 9, and 12 months for El Niño event R5 and a start month of October (−1), which are caused by the corresponding CNOP error. The CNOP error of this prediction experiment belongs to the type-2 CNOP error in Figure 2, with one negative pole in the equatorial eastern Pacific and one positive pole in the equatorial central Pacific. The error evolution of SSTA in Figure 3a shows that the negative pole develops strongly, while the positive pole decays gradually and disappears after 6 months, replaced by the intensified negative SSTA error. The dramatic increase in the magnitude of the negative SSTA error can be traced back to the significantly large error of the wind anomaly over the equatorial Pacific. In fact, at a lead time of 6 months, an obvious error in the easterly wind anomaly appears at around 120°W–140°W (Figure 3b). This error can be considered as an easterly wind perturbation, and it influences the thermocline depth anomalies and upwelling in the eastern Pacific via the propagation of equatorial oceanic waves and Ekman pumping, consequently influencing SSTA by means of thermocline depth feedback and upwelling feedback [*Dijkstra*, 2005].

[14] Figure 3c shows the response of thermocline depth anomalies to the wind perturbation. The signals located west and east of the wind perturbations are attributed to the Rossby waves and Kelvin waves, respectively. The shoaling of thermocline depth anomalies in the eastern Pacific is favorable for the entrainment of colder subsurface water, leading to an enhanced negative error of SSTA in this area. Figure 3 shows that the evolution of CNOP error can be explained by Bjerknes feedback. To a certain extent, the CNOP error enhances this feedback because it leads to the largest prediction error at the prediction time

3. The Location of Initial Errors

[15] The CNOP error comprises relatively large values of initial SSTA error in the equatorial central and eastern Pacific and small values in other regions, and it causes the largest prediction error at the prediction time, according to the definition of CNOP. Prior to assessing the effect of the initial error in the equatorial central and eastern Pacific, the domain of the ZC ocean model is divided into six parts with equal numbers of grid points (Domain i (i = 1, …, 6) in Figure 2). Domain 5, where the dipole pattern of SSTA error with large values is mainly located, is defined as the sensitive area (157.5°W–90°W, 5°S–5°N) covering the equatorial central and eastern Pacific. It is supposed that initial errors in Domain 5 evolve more significantly than those in other domains. To test this assumption, we compute the maximal predication errors caused by initial error confined within each of the six domains. The cost function is still defined as

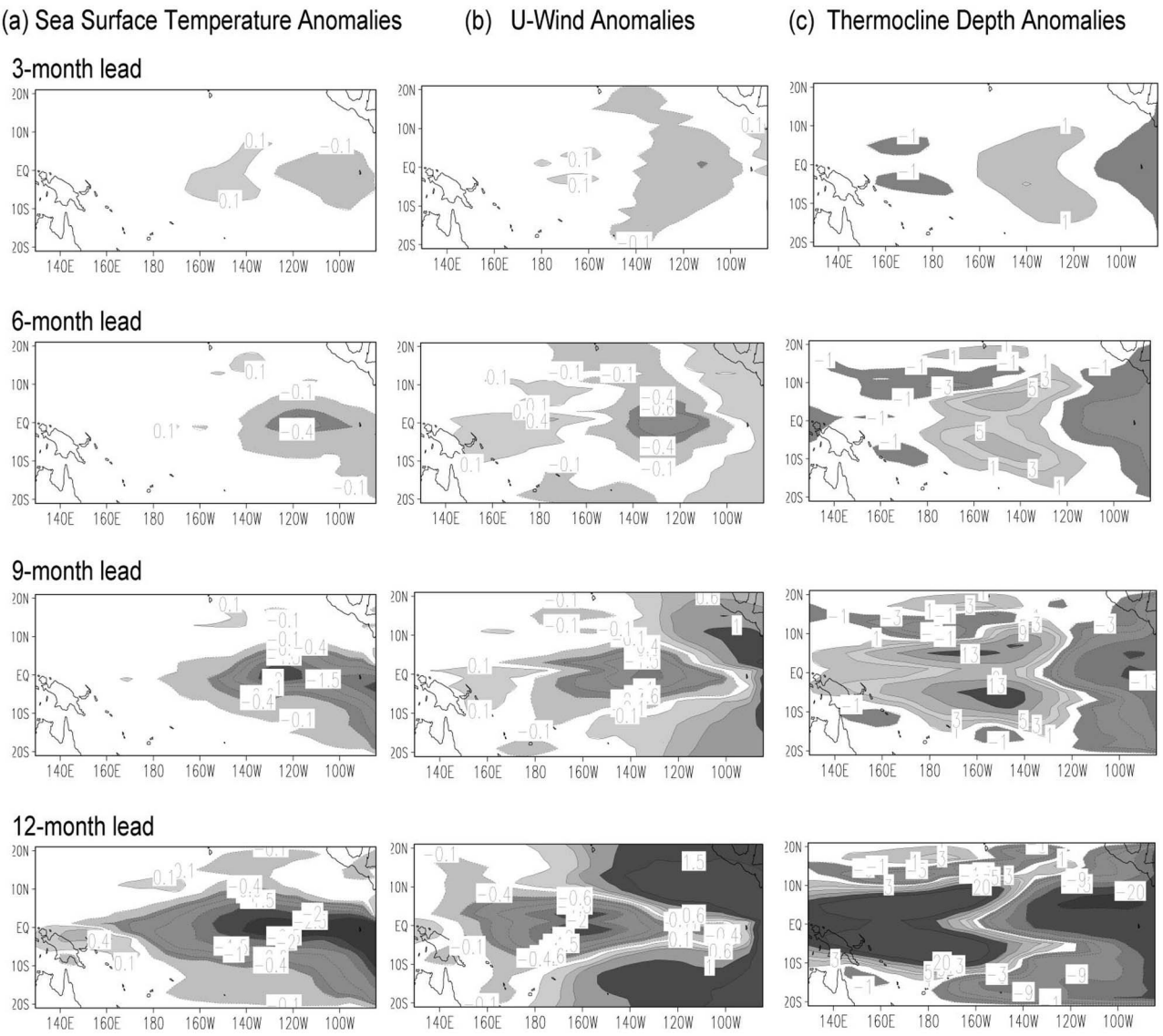

Figure 3. Prediction errors of (a) SSTA, (b) zonal wind anomalies, and (c) thermocline depth anomalies caused by CNOP error for El Niño event R5 and a start month of October (−1).

equation (1) to measure the evolution of the initial error of SSTA at the prediction time, but the constraint condition $\|\vec{T}'_0\|_2 \le \delta$ is defined by another positive real number δ and the norm $\|\vec{T}'_0\|_2 = \sqrt{\sum_{i,j} T'^2_{0i,j}}$, where $T'_{0i,j}$ represents the initial error of the SSTA and (i, j) the interior grid point in the one of six domains. Because the number of grid points in each domain is 1/6 of the total grid points in section 2, the δ is determined as 0.49 in this section. For 8 El Niño events and 12 start months, we make 576 ($12 \times 8 \times 6$) optimization experiments. Figure 4 shows the obtained 6 CNOP errors and their corresponding cost functions for El Niño R5 and a start month of October (−1). It can be seen that clearly dipole patterns of SSTA errors are found in Domain 4, Domain 5, and Domain 6, which are all located in the eastern Pacific. This implies that the dipole pattern of SSTA error is more likely to appear in the eastern Pacific other than western Pacific. Furthermore, it is the CNOP error in Domain 5 that causes the maximum value of the cost function among these 6 CNOP errors. The averaged cost functions for 96 (12×8) optimization experiments for each domain are listed in Table 1, which also confirms the above result.

[16] The initial errors evolve more strongly in the sensitive area (Domain 5) than in other regions, which can be explained as follows. *Yu et al.* [2009] reported that the mechanism of the evolution of the ENSO signal could be used to explain the error growth, and that Bjerknes positive feedback is responsible for error growth. Therefore, it is supposed that the reason for the strongest ENSO signal occurs in the equatorial central and eastern Pacific may also explain why the location of the sensitive area of error growth is in this region. Because of the easterly trade wind along the equator and the resultant mean upwelling in the eastern Pacific, the thermocline is shallower in this region than within the equatorial western Pacific. The shallower thermocline in the equatorial eastern Pacific favors the influence of a variable thermocline on the development of SSTA by

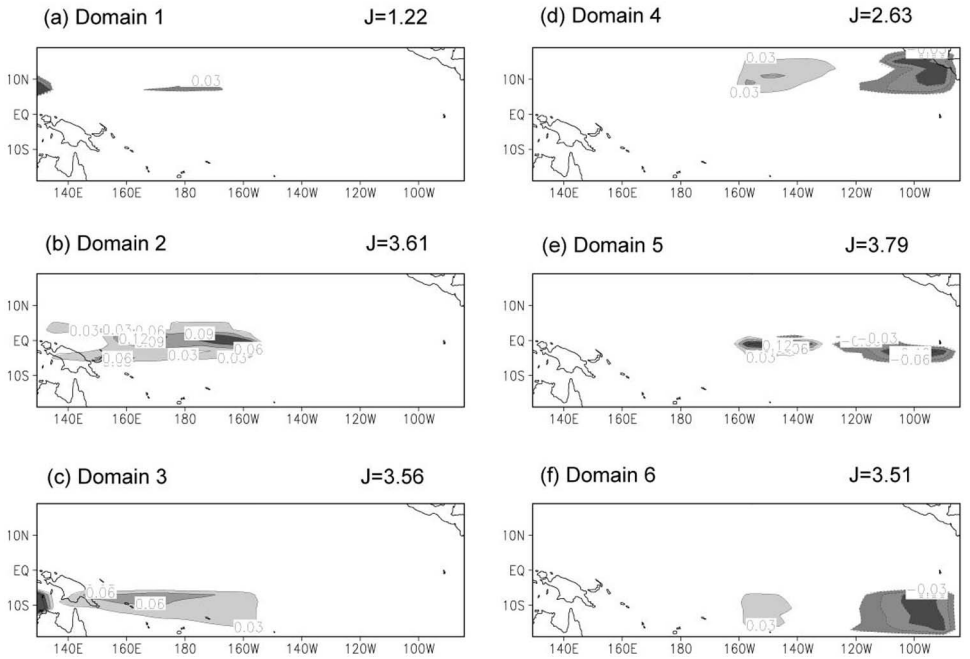

Figure 4. (a–f) For El Niño R5 and a start month of October (−1), 6 CNOP errors located in 6 domains are shown respectively, together with 6 values of cost functions.

means of upwelling or downwelling. The importance of the location of initial errors represents the effects of reference states, and in this context it is the space-dependent climatological mean thermocline depth that affects the error evolution. The dipole pattern of CNOP error located in the equatorial central and eastern Pacific acts as a trigger of Bjerknes positive feedback. Weaker (stronger) easterly trade wind over the dipole induces downwelling (upwelling) Kelvin waves that act to weaken (intensify) the upwelling in the equatorial eastern Pacific, where the shallow thermocline favors thermocline–SST feedback. Consequently, the positive (negative) initial error of SSTA in the Niño-3 region is amplified, causing a significant prediction error of Niño-3 indices and resulting in overestimation (underestimation) of the strength of El Niño events.

4. The Spatial Pattern of Initial Errors

[17] As can be seen in the previous section, the equatorial central and eastern Pacific is the most important locations for initial error growth. In this section, we examine the effect of the spatial pattern of initial errors on El Niño prediction.

[18] First, we consider initial random errors that spread over the sensitive area with the same magnitude as the CNOP error in this area, assuming that the initial random error at each grid point is unbiased. For a particular El Niño event and start month, one initial random error field is constructed within the sensitive area (Domain 5). The value of the random error at a particular grid point $T'_{ri,j}$, where the subscript i, j denotes the grid point within Domain 5, is chosen from a random sequence of real numbers with a normal distribution and a randomly given variance. The values of this initial field at different grid points are chosen from different random series with various variances. The magnitude of the random field should be scaled to be equal to that of the corresponding CNOP error within Domain 5 for fair comparison. The magnitude of the random error is measured by the L2 norm $||\vec{T}'_r||_2 = \sqrt{\sum_{i,j} T'^2_{r\,i,j}}$. Hence, we scale the random error field $\vec{T}'_r$ with $\sigma\frac{\vec{T}'_r}{||\vec{T}'_r||_2}$, where σ is a positive real number. We make σ identical to the magnitude of the corresponding CNOP error within this domain, and then obtain a scaled random initial error $\vec{T}'_{r\,0} = \sigma\frac{\vec{T}'_r}{||\vec{T}'_r||_2}$ with the magnitude $||\vec{T}'_{r\,0}||_2 = \sigma$. This scaled random error is then superimposed on the corresponding El Niño event at the start month, and the ZC model is integrated for 1 year.

[19] For 8 El Niño events and 12 start months, a total of 96 prediction experiments are performed, and the averaged absolute value of the prediction error of Niño-3 indices at the prediction time, as caused by the random initial errors, is 0.052°C, much smaller than the averaged absolute values of prediction errors caused by CNOP errors within Domain 5, which is 0.621°C. It is clear that the random initial errors located in the sensitive area (Domain 5) yield small

Table 1. Averaged Cost Functions Among 96 Optimization Experiments in Domain i (i = 1, …, 6)

	Domain 1	Domain 2	Domain 3	Domain 4	Domain 5	Domain 6
Averaged cost function	1.06	2.47	1.50	1.27	3.24	2.19

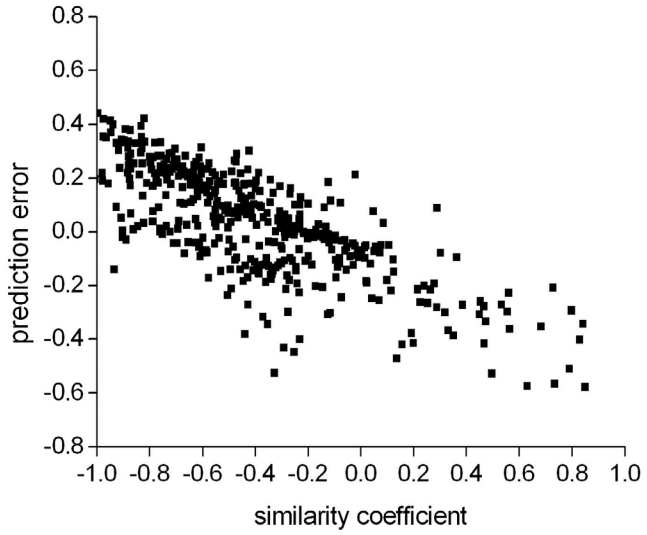

Figure 5. Relationship between prediction errors of Niño-3 indices caused by initial errors and similarity coefficients, which are computed between each of 240 initial errors and the CNOP error for El Niño event R5 and a start month of October (−1).

prediction uncertainties compared with those resulting from the CNOP error within the same area. Given the lack of a particular dipole pattern of SSTA, random initial errors with the same magnitude as the CNOP error will not evolve significantly, even when located in the sensitive area defined by large values of CNOP error.

[20] In real operational predictions, the initial error is not simply a random error: it possesses a particular spatial pattern due to initialization of the model and may differ in magnitude from the CNOP error. Consequently, we considered other initial errors with a given spatial pattern derived from analysis data sets, to evaluate the impact of the spatial pattern of the initial error on the prediction error. Differences within the sensitive area (Domain 5) between two monthly mean data sets—the initial conditions of SSTA used in the hindcast experiment of LDEO5 (the latest version of the ZC model) [*Chen et al.*, 2004] and Kaplan extended version2 SSTA [*Kaplan et al.*, 1998; *Reynolds and Smith*, 1994]—from January in 1980 to December in 1999 are considered as 240 initial analysis errors, and subsequently are superimposed on each predetermined model El Niño event at each start month. After calculating the prediction errors caused by these initial errors at the prediction time, we note that for a given El Niño event and start month, some initial errors cause non-negligible prediction errors, whereas others induce trivial errors. It is supposed that the spatial pattern of the former initial errors is similar to that of the corresponding CNOP error related to the El Niño event and start month. Thus, we calculated the similarity coefficient between each initial error and the CNOP error within the sensitive area.

[21] Figure 5 compares the similarity coefficient and prediction errors of Niño-3 indices for El Niño event R5 and a start month of October (−1), revealing that the initial errors that possess similar spatial patterns to the CNOP error tend to cause larger prediction errors. Other El Niño events and start months yield similar results (data not shown). In the case that the similarity coefficients are negative, the larger absolute value of similarity coefficients coincide with larger prediction errors, due to the existence of local CNOP error. The CNOP error for this El Niño event and start month corresponds to a type-2 CNOP error (see Figure 2), causing a negative prediction error for the Niño-3 index. The corresponding local CNOP error for this El Niño event and start month is similar to the type-1 CNOP error in Figure 2. When the initial error is similar to the local CNOP error, the similarity coefficient between the initial error and the CNOP error is negative, but it could still cause a non-negligible prediction error.

[22] Our analysis of the error evolution of an initial random error and an initial error with various spatial patterns (as obtained from analysis data sets) reveals that the spatial pattern of the initial error plays an important role in determining the prediction error: the initial error evolves more strongly in the case that it possesses a similar spatial pattern to that of the CNOP error, which possesses a dipole pattern of SSTA in the central and eastern equatorial Pacific (Domain 5). To further investigate how essential the dipole pattern of CNOP error is, we present the evolution of central part and eastern part of the dipole separately for El Niño R5 and a start month of October (−1) in Figure 6. In the left column, it is shown that the positive central part of the dipole disappears after 6 months, while a negative prediction error appears to the east of the original central part at the lead time of 6 months and evolves stronger gradually. The prediction error attains −0.6°C at the lead time of 12 months. In the middle column, it can be seen that the negative eastern part of the dipole grows much stronger and faster, attaining −1.0°C after 12-month evolution. For this case, the eastern part evolves more significantly than the central part. When both two exist, the prediction error could attain −2.5°C, much stronger than the linear combination of prediction errors caused by central part and eastern part separately. It means that the nonlinearity plays a non-negligible role in the error evolution in this case. However, the nonlinearity could be neglected for some cases, especially when the magnitude of prediction error is small. Figure 7 presents a case which corresponds to El Niño R7 and a start month of July (−1). For this case, the prediction error caused by the dipole pattern is approximately equal to the linear combination of prediction errors caused by two parts separately. Besides, the prediction errors are significantly smaller than that of the case in Figure 6. It should be noted that although the positive central part disappears after 3 months with a negative prediction error appearing to the east, its evolution after 12 months is larger than the prediction error evolved from the eastern part directly, which is also different from the case in Figure 6. The relative importance of the central part and the eastern part remains unclear and needs further study in the future.

5. Implications for Targeted Observations

[23] Section 4 showed that the initial error in the sensitive area (Domain 5) causes a larger prediction error if it possesses a similar spatial pattern to that of the corresponding CNOP error related to the given El Niño event and start month. We infer that when an initial error, considered as a

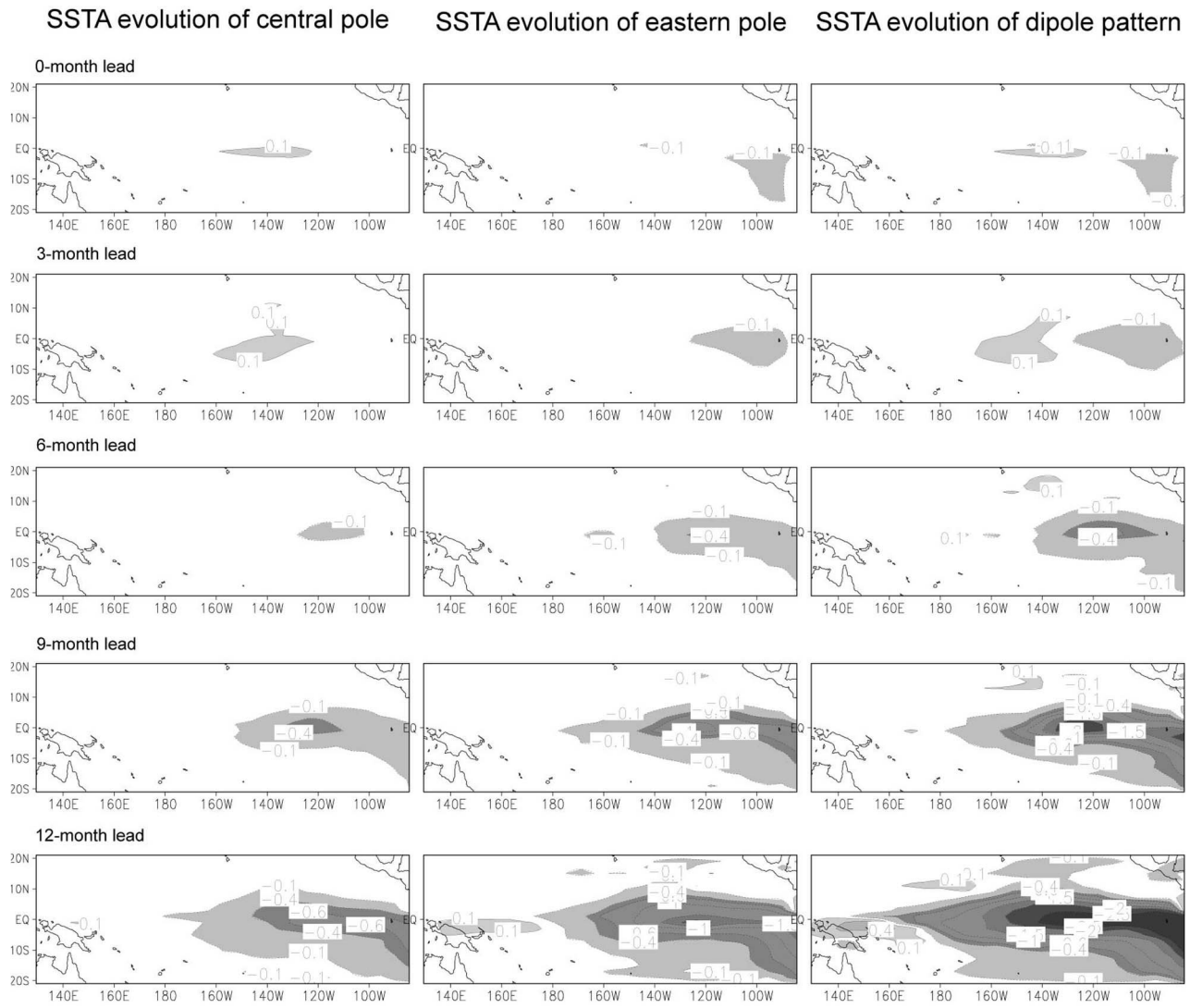

Figure 6. The time-dependent prediction error of SSTA evolved from (left) central pole, (middle) eastern pole, and (right) dipole pattern of CNOP error related to El Niño R5 and a start month of October (−1).

vector, is decomposed into two vectors—one parallel to the direction of the CNOP error (i.e., the projection of the initial error onto the CNOP error) and the other orthogonal to it, denoted by Component I and Component II, respectively. Let $\vec{E}_u, \vec{E}_c, \vec{E}_1, \vec{E}_2$ be the undecomposed initial error, CNOP error, Component I and Component II, then $\vec{E}_1 = \frac{\vec{E}_u \bullet \vec{E}_c}{\vec{E}_c \bullet \vec{E}_c}\vec{E}_c$, $\vec{E}_2 = \vec{E}_u - \vec{E}_1$. Here, we decompose each of the initial errors which are constructed from Kaplan extended version2 SSTA and initial condition of SSTA used in the hindcast of LDEO5 as in Section 4, except covering the whole model domain, into the two components and compute their respective evolutions.

[24] Figure 8 shows the root-mean-square error (RMSE) in the Niño-3 region caused by these two components of initial errors, revealing that although the magnitude of the projection of the initial error onto the CNOP error (i.e., Component I) is significantly smaller than that of the other component at the initial time, the growth rate is much higher; consequently, the two prediction errors are comparable in magnitude after 1 year. Also shown in Figure 8 is the RMSE in the Niño-3 region caused by the undecomposed initial error. The significant growth of the undecomposed error during the first 6 months can be attributed to the obvious growth of Component I. Therefore, we conclude that it is Component I, as a fraction of initial error at start month, that accounts for the error growth.

[25] Although it appears that eliminating the projection of the initial error on the CNOP error (i.e., Component I) would be helpful in improving the prediction skill, in the realistic predictions it is not possible to identify the true initial error; consequently, it is not possible to eliminate Component I from the initial error. A compromise strategy would be to prevent the occurrence of the CNOP error in the initial condition. We have shown that large values of CNOP error in the equatorial central and eastern Pacific result in significant prediction errors. This finding raises the possibility of improving the forecast skill by reducing the initial error within the sensitive area, which could be achieved by additional targeted observations in this area. In this section,

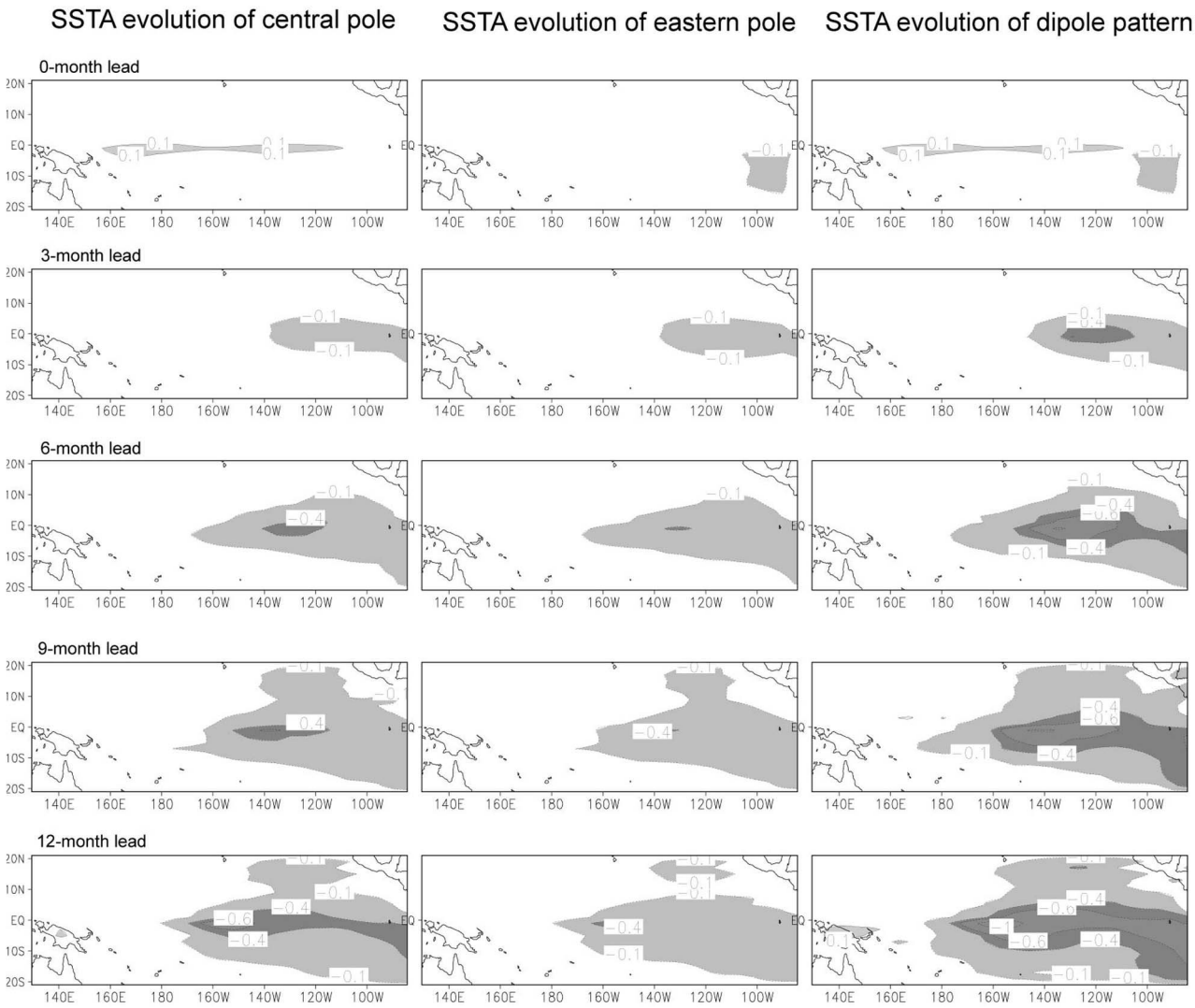

Figure 7. The same as Figure 6 but for El Niño R7 and a start month of July (−1).

we examine the extent to which the prediction results are improved by eliminating the initial error in several predetermined areas, including the sensitive area.

[26] A set of initial errors, consisting of 240 members (referred to as original initial errors in this context), was constructed in the same way as in the previous section, except covering the entire domain of the ZC model, representing the differences between the two monthly mean data sets from January 1980 to December 1999. These initial errors are superimposed on each predetermined El Niño event at each start month, followed by computation of the prediction errors of SSTA during a calendar year caused by these initial errors. Hence, a total of 240 × 96 prediction experiments were performed. Note that the reference "true" states are still the eight El Niño model events described in Section 2; no observational data are used as "true" states.

[27] Figure 9 shows the time-dependent RMSE of SSTA in the Niño-3 region over all the prediction experiments (black line). The initial errors develop gradually and cause non-negligible prediction errors after 1 year, despite damping during the first month due to imbalance among the different model variables (e.g., SSTA, thermocline depth anomalies, and wind anomalies).

[28] To examine the effect of reducing initial errors in different areas on prediction errors, for each original initial error field, six subsets are generated by eliminating its component in domain i (i = 1 … 6, as described in section 3) from the full initial error. Six sets of ideal numerical experiments are then performed with these new initial error fields, accordingly they are denoted by Exp i. For each subset, there are totally 240 original initial error fields, which are derived as the differences between two monthly mean data sets (see section 4). Prediction errors caused by these each set of new initial errors are computed in Exp i, and the RMSE of the Niño-3 SSTA for each set of new initial errors is plotted in Figure 9. By eliminating the initial errors of SSTA in the sensitive area (Domain 5), without changing the initial errors of SSTA in other regions, the prediction results are improved after 1 year in Exp 5 (purple line). Because the Niño-3 region is located in Domain 5,

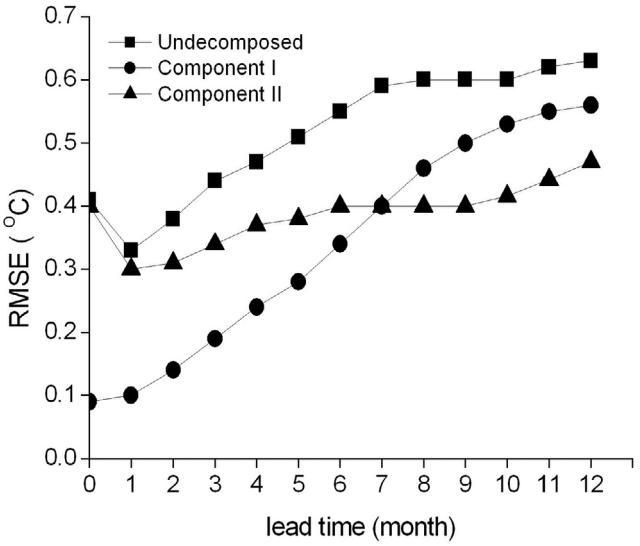

Figure 8. Root-mean-square error for Niño-3 SSTA caused by undecomposed initial errors and their two components. Component I denotes the projection of the initial error on the direction of the CNOP error, and Component II is undecomposed initial error minus Component I.

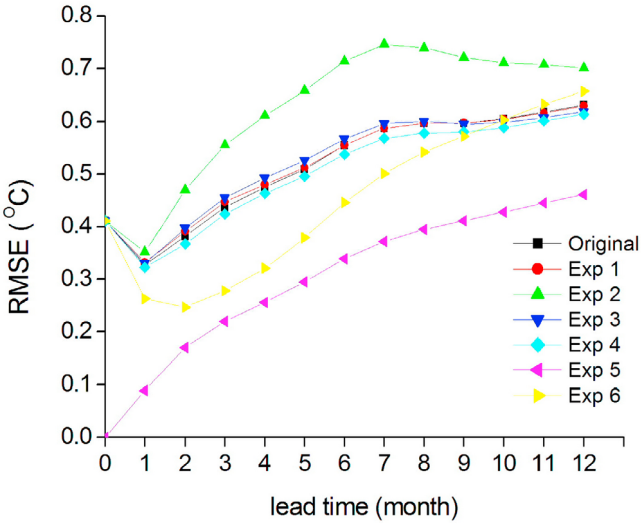

Figure 9. Root-mean-square error for Niño-3 SSTA caused by the original initial errors (black line) and six other sets of initial errors. Each set of new initial errors is generated by eliminating errors in one of the six domains from the original initial errors.

eliminating the initial error in Domain 5 means that the RMSE in the Niño-3 region is zero at the initial time. Eliminating the initial errors of SSTA in Domain 6 also enhances the prediction skill within 6 months, but the effects become increasingly weak over time. It might seem surprising that eliminating the initial errors in any one of the other four areas does not enhance the prediction skill obviously. We suppose that the initial errors in the sensitive area account for the bulk of the prediction errors. If the initial errors in the sensitive area are not changed at the initial time, they will generate large prediction errors, regardless of whether the initial errors are eliminated in any of the other areas.

[29] Specially, removing the initial SSTA errors in the equatorial western Pacific (i.e., Exp 2) actually worsen the prediction significantly, causing larger RMSE than that of the original case in which all initial error components are retained (green line and black line). This could be attributed to the opposite effects of initial errors in equatorial western Pacific and eastern Pacific on the signs of prediction errors of Niño-3 indices. To focus on only the worst prediction cases in Exp 2, we narrow down the total 240*96 samples to 500 forecast members, which lead to the largest 500 values of RMSE in the forecasts. The corresponding prediction errors of Niño-3 indices for the selected 500 tests from Exp 2 are examined. We also look at the prediction errors of Niño-3 indices for the same 500 initial error patterns but excluding their components in sensitive area Domain 5 this time. The scatter points of prediction errors of Niño-3 indices for the 500 selected samplings in Exp 2 and Exp 5 are plotted in Figure 10. For selected Exp 2 tests, the prediction errors of Niño-3 indices range from -3°C to -1°C. Meanwhile, the majority of the scatter points show positive values in Exp 5 case, which suggests that given the same initial error field, Domain 2 initial errors may cancel the effect by Domain 5 initial errors on predictions by some amount. Therefore, keeping the full initial errors actually reduces the predictions errors than Exp 2 case, since the initial errors in equatorial western Pacific and eastern Pacific cause competing effects on El Niño prediction. We try to present a scenario accompanying Figure 10 to describe the

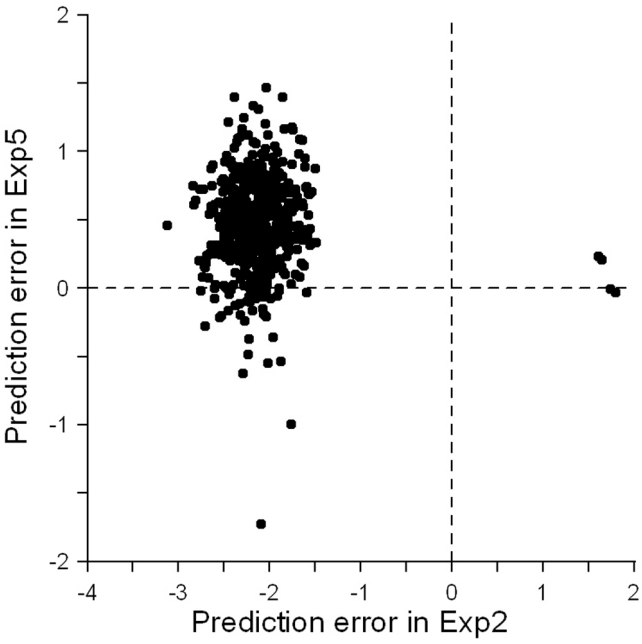

Figure 10. Scatterplot of prediction errors of Niño-3 indices for the 500 selected samplings in Exp 2 and Exp 5.

above explanation more clearly. It is supposed that there is a dipole pattern of initial error of SSTA in Domain 5 with a positive part in the central equatorial Pacific and a negative part in the eastern equatorial Pacific, which will cause easterly anomalies and a significant negative prediction error in Niño-3 area after 1-year evolution according to our discussion in Section 4; there is also a negative value of SSTA error in the Domain 2, which will cause westerly anomalies in central Pacific and subsequent positive prediction error of SSTA in Niño-3 region. Because the initial error in Domain 5 grow more significantly than initial error in Domain 2, as we discussed in Section 3, the sign of prediction error by coexisting initial errors in both domains is negative and the magnitude of prediction error is smaller than that caused by initial error in Domain 5. Of course, this is only one explanation for the occurrence of worse forecast skill caused by more accurate information in Domain 2, it might also be due to the imbalance of different variables after elimination of initial error in Domain 2.

[30] As we stated in the introduction, the accuracy of SST data is far from perfect although advances in technology in recent years greatly improved the performances of the satellite sensors observing the ocean temperature. There are some limitations to the accuracy of these satellite observations. One way of improving accuracy of satellite SST data is to increase in situ observations. For example, SST algorithm coefficients of infrared satellite are often found by regression of the satellite radiances against in situ bulk SST (0.5 to 5 m below the sea surface). To improve the accuracy of satellite SST, *Emery et al.* [2001] suggested that in situ skin SST (approximately 10 μm within oceanic skin layer) is more appropriate than in situ bulk SST for calculating satellite SST algorithm coefficients; while a lack of measurements of in situ skin SST had led to the common SST estimation practice to adjust the satellite SST to match a selection of in situ bulk SST. They claimed that more simultaneous measurements of in situ skin and bulk SST by ships of opportunity, moored and drifting buoys could be provided to validate and modify satellite SST measurements; with these validation measurements, it should be possible to achieve an SST accuracy of 0.1–0.3 C for both bulk and skin SST. *Donlon et al.* [2007] also suggested that a combination of independent SST retrievals from in situ and space-based sensors using different methodology is one effective way to reduce the scientific limitations on SST retrievals and increase their accuracy. They tried to achieve one of the objectives of Global Ocean Data Assimilation Experiment High-Resolution SST Pilot Project, which is to develop a new generation of SST data obtained by blending multisensor retrievals. All these studies demonstrate that more observations by ships of opportunity, moored and drifting buoys could contribute to obtain a more accurate SST data. The results of our numerical experiments indicate that reducing the initial errors of SSTA in the sensitive area would improve the forecast skill in El Niño predictions to some extent. Due to the expensive cost of deploying moored and drifting buoys in ocean, in the case that additional observation instruments are made available to increase the accuracy of SST within a limited area, they should be deployed in the sensitive area rather than elsewhere. Note that there are circumstances that additional observational data in some regions might decrease the forecast skill. This suggests that additional observations should be deployed more carefully in the case that initial errors in different areas play opposite effects on prediction errors systematically in forecast experiments.

6. Summary

[31] Given the location of large CNOP errors in the equatorial central and eastern Pacific and the dipole pattern of SSTA, we investigated the contribution of the location and spatial pattern of this type of initial error to the error evolution in El Niño prediction experiments. The equatorial central and eastern Pacific (Domain 5) was compared with five other regions in terms of the effects of initial errors confined in each of regions on prediction errors. Through the calculation of the maximal cost functions measuring prediction errors caused by initial errors from different domains, we find that initial errors in Domain 5 evolve more significantly than those in other domains. It is supposed that the reason for the strongest ENSO signal occurs in the equatorial central and eastern Pacific may also explain why the location of the sensitive area of error growth is in this region. The shallow thermocline depth in this region enhances the influence of subsurface water on SSTA by means of vertical advection. The importance of the location of the initial error demonstrates the effect of the climatological mean state on error evolution.

[32] The spatial pattern of initial errors also plays an important role in the error evolution. An initial random error in the predetermined sensitive area cannot trigger non-negligible prediction errors. We also considered initial errors with certain spatial patterns, as obtained from the initial conditions of the LDEO5 hindcast experiment and reanalysis data. An initial error with a spatial pattern similar to that of the CNOP error tends to cause a larger prediction error. The dipole pattern of the initial error of SSTA in the eastern Pacific acts to trigger Bjerknes positive feedback. The central part of the dipole disappears after several month evolution, and it cause a prediction error of SSTA with opposite sign to the east, which grows gradually afterwards. The eastern part of the dipole grows all the time and doesn't change its sign. If the magnitude of prediction error is large, the prediction error caused by the dipole pattern cannot be considered as a simple linear combination of prediction errors caused by each part of dipole separately, which means nonlinearity plays an important role in the error evolution.

[33] Considering the importance of the similarity coefficient between the initial error and the CNOP error, we decomposed the initial error into two components (one parallel to the direction of the CNOP error and the other orthogonal to it) and assessed their respective influences on the prediction errors. The projection of initial error on the direction of the CNOP error at the start month, just only a small fraction of initial error, accounts for the error growth in the following 12 months. However, in practical predictions it is not possible to eliminate this small fraction from the initial error.

[34] A compromise strategy is to prevent the occurrence of CNOP error in the initial conditions. Additional observations of SST in the sensitive area could reduce the initial error of SST, and is expected to improve forecast skill. Our

experiment results confirm that this method could reduce prediction errors to some extent. In the case that additional observation instruments are only capable of covering a limited area, they should be implemented in the sensitive area rather than other regions. Note that there are circumstances that additional observational data in some regions might decrease the forecast skill. It could be attributed to the systematically opposite effects of initial errors located in two areas on prediction errors in forecast experiments. Removing initial error in one area that is not the most sensitive area could actually worsen the prediction results. This shows the importance of finding the most sensitive area and suggests that additional observations should be deployed more carefully in this case.

[35] This paper presents the results of a preliminary study of targeted observations related to ENSO predictions, using information provided by the CNOP error. Of course, the model adopted here may be relatively simple and may not consider the complete physics of a coupled ENSO. The results may therefore be limited in regards to the model's ability to simulate a real system. Hence, the understanding gained from the present study needs further verification using models with more complete physics. The application of more complex models for ENSO prediction would enable the delineation of a 3-D sensitive region, which would be an advance on analyses of a 2-D region. It will provide a more accurate sensitive area, including subsurface information, other than our current simple sensitive area defined as a rectangle in the eastern equatorial Pacific. In that case, it will help to implement subsurface observation to improve our forecast skill. In addition, one of the challenges in ENSO forecasting is also in avoidance of false predictions of El Niño events. This work is focused on the analysis of El Niño events that do occur, from the view of hindcast experiments. Whether the targeted observation will reduce the occurrence of false prediction of El Niño event needs further studies.

[36] **Acknowledgments.** The authors thanks Youmin Tang and Yanjie Cheng for kindly providing initial conditions of SSTA used in the LDEO5 hindcast experiment. This work was jointly sponsored by the National Basic Research Program of China (2010CB950402, 2012CB955202), the Knowledge Innovation Program of the Chinese Academy of Sciences (KZCX2-YW-QN203), the National Nature Scientific Foundation of China (41006015,41176013), and the Basic Research Program of Qingdao Scientific and Technological Plan (111495jch).

References

Birgin, E. G., J. M. Martínez, and M. Raydan (2000), Nonmonotone spectral projected gradient methods on convex sets, *SIAM J. Optim.*, *10*, 1196–1211, doi:10.1137/S1052623497330963.

Cai, M., E. Kalnay, and Z. Toth (2003), Bred vectors of the Zebiak-Cane model and their potential application to ENSO predictions, *J. Clim.*, *16*, 40–56, doi:10.1175/1520-0442(2003)016<0040:BVOTZC>2.0.CO;2.

Castro, S., G. A. Wick, D. L. Jackson, and W. J. Emery (2008), Error characterization of infrared and microwave satellite sea surface temperature products for merging and analysis, *J. Geophys. Res.*, *113*, C03010, doi:10.1029/2006JC003829.

Chen, D., and M. Cane (2008), El Niño prediction and predictability, *J. Comput. Phys.*, *227*, 3625–3640, doi:10.1016/j.jcp.2007.05.014.

Chen, D., M. A. Cane, A. Kaplan, S. E. Zebiak, and D. Huang (2004), Predictability of El Niño over the past 148 years, *Nature*, *428*, 733–736, doi:10.1038/nature02439.

Chen, Y. Q., D. S. Battisti, R. N. Palmer, J. Barsugli, and E. Sarachik (1997), A study of the predictability of tropical Pacific SST in a coupled atmosphere/ocean model using singular vector analysis, *Mon. Weather Rev.*, *125*, 831–845, doi:10.1175/1520-0493(1997)125<0831:ASOTPO>2.0.CO;2.

Cheng, Y., Y. Tang, X. Zhou, P. Jackson, and D. Chen (2010a), Further analysis of singular vector and ENSO predictability in the Lamont model—Part I: Singular vector and the control factors, *Clim. Dyn.*, *35*, 807–826, doi:10.1007/s00382-009-0595-7.

Cheng, Y., Y. Tang, P. Jackson, D. Chen, X. Zhou, and Z. Deng (2010b), Further analysis of singular vector and ENSO predictability from 1856–2003—Part II: Singular value and predictability, *Clim. Dyn.*, *35*, 827–840, doi:10.1007/s00382-009-0728-z.

Dijkstra, H. A. (2005), *Nonlinear Physical Oceanography: A Dynamical Systems Approach to the Large Scale Ocean Circulation and El Niño*, 532 pp., Springer, Dordrecht, Netherlands.

Donlon, C., et al. (2007), The Global Ocean Data Assimilation Experiment High-Resolution Sea Surface Temperature Pilot Project, *Bull. Am. Meteorol. Soc.*, *88*, 1197–1213, doi:10.1175/BAMS-88-8-1197.

Duan, W. S., and M. Mu (2006), Investigating decadal variability of El Nino–Southern Oscillation asymmetry by conditional nonlinear optimal perturbation, *J. Geophys. Res.*, *111*, C07015, doi:10.1029/2005JC003458.

Duan, W. S., and M. Mu (2009), Conditional nonlinear optimal perturbation: Applications to stability, sensitivity, and predictability, *Sci. China D*, *52*, 883–906, doi:10.1007/s11430-009-0090-3.

Duan, W. S., and C. Wei (2012), The "spring predictability barrier" for ENSO predictions and its possible mechanism: Results from a fully coupled model, *Int. J. Climatol.*, in press.

Duan, W. S., M. Mu, and B. Wang (2004), Conditional nonlinear optimal perturbations as the optimal precursors for El Nino–Southern Oscillation events, *J. Geophys. Res.*, *109*, D23105, doi:10.1029/2004JD004756.

Duan, W. S., H. Xu, and M. Mu (2008), Decisive role of nonlinear temperature advection in El Nino and La Nina amplitude asymmetry, *J. Geophys. Res.*, *113*, C01014, doi:10.1029/2006JC003974.

Duan, W. S., X. C. Liu, K. Y. Zhu, and M. Mu (2009), Exploring the initial error that causes a significant spring predictability barrier for El Nino events, *J. Geophys. Res.*, *114*, C04022, doi:10.1029/2008JC004925.

Emery, W. J., S. Castro, G. A. Wick, P. Schluessel, and C. Donlon (2001), Estimating sea surface temperature from infrared satellite and in situ temperature data, *Bull. Am. Meteorol. Soc.*, *82*, 2773–2785, doi:10.1175/1520-0477(2001)082<2773:ESSTFI>2.3.CO;2.

Gebbie, G., I. Eisenman, A. Wittenberg, and E. Tziperman (2007), Modulation of westerly wind bursts by sea surface temperature: A semistochastic feedback for ENSO, *J. Atmos. Sci.*, *64*, 3281–3295, doi:10.1175/JAS4029.1.

Gentemann, C. L., F. J. Wentz, C. A. Mears, and D. K. Smith (2004), In situ validation of Tropical Rainfall Measuring Mission microwave sea surface temperatures, *J. Geophys. Res.*, *109*, C04021, doi:10.1029/2003JC002092.

Harris, A. R., and M. A. Saunders (1996), Global validation of the along-track scanning radiometer against drifting buoys, *J. Geophys. Res.*, *101*, 12,127–12,140, doi:10.1029/96JC00317.

Jin, E. K., et al. (2008), Current status of ENSO prediction skill in coupled ocean-atmosphere models, *Clim. Dyn.*, *31*, 647–664, doi:10.1007/s00382-008-0397-3.

Jin, F. F., J. D. Neelin, and M. Ghil (1994), El Niño on the devil's staircase: Annual subharmonic steps to chaos, *Science*, *264*, 70–72, doi:10.1126/science.264.5155.70.

Kaplan, A., M. Cane, Y. Kushnir, A. Clement, M. Blumenthal, and B. Rajagopalan (1998), Analyses of global sea surface temperature 1856–1991, *J. Geophys. Res.*, *103*(C9), 18,567–18,589, doi:10.1029/97JC01736.

Kearns, E. J., J. A. Hannifin, R. H. Evans, P. J. Minnett, and O. B. Brown (2000), An independent assessment of Pathfinder AVHRR sea surface temperature accuracy using the Marine Atmosphere Emitted Radiance Interferometer (MAERI), *Bull. Am. Meteorol. Soc.*, *81*, 1525–1536, doi:10.1175/1520-0477(2000)081<1525:AIAOPA>2.3.CO;2.

Kleeman, R., and A. M. Moore (1997), A theory for the limitation of ENSO predictability due to stochastic atmospheric transients, *J. Atmos. Sci.*, *54*, 753–767, doi:10.1175/1520-0469(1997)054<0753:ATFTLO>2.0.CO;2.

Langland, R. H. (2005), Issues in targeted observing, *Q. J. R. Meteorol. Soc.*, *131*(613), 3409–3425, doi:10.1256/qj.05.130.

Luo, J. J., S. Masson, S. Behera, and T. Yamagata (2008), Extended ENSO predictions using a fully coupled ocean-atmosphere model, *J. Clim.*, *21*, 84–93, doi:10.1175/2007JCLI1412.1.

Moore, A. M., and R. Kleeman (1996), The dynamics of error growth and predictability in a coupled model of ENSO, *Q. J. R. Meteorol. Soc.*, *122*, 1405–1446, doi:10.1002/qj.49712253409.

Moore, A. M., J. Zavala-Garay, Y. Tang, R. Kleeman, A. T. Weaver, J. Vialard, K. Sahami, D. L. T. Anderson, and M. Fisher (2006), Optimal forcing patterns for coupled models of ENSO, *J. Clim.*, *19*, 4683–4699, doi:10.1175/JCLI3870.1.

Morss, R. E., and D. S. Battisti (2004a), Designing efficient observing networks for ENSO prediction, *J. Clim.*, *17*, 3074–3089, doi:10.1175/1520-0442(2004)017<3074:DEONFE>2.0.CO;2.

Morss, R. E., and D. S. Battisti (2004b), Evaluating observing requirements for ENSO prediction: Experiments with an intermediate coupled model, *J. Clim.*, *17*, 3057–3073, doi:10.1175/1520-0442(2004)017<3057:EORFEP>2.0.CO;2.

Mu, M., and W. S. Duan (2003), A new approach to studying ENSO predictability: Conditional nonlinear optimal perturbation, *Chin. Sci. Bull.*, *48*, 1045–1047.

Mu, M., W. S. Duan, and B. Wang (2003), Conditional nonlinear optimal perturbation and its applications, *Nonlinear Processes Geophys.*, *10*, 493–501, doi:10.5194/npg-10-493-2003.

Mu, M., L. Sun, and D. A. Henk (2004), The sensitivity and stability of the ocean's thermocline circulation to finite amplitude freshwater perturbations, *J. Phys. Oceanogr.*, *34*, 2305–2315, doi:10.1175/1520-0485(2004)034<2305:TSASOT>2.0.CO;2.

Mu, M., H. Xu, and W. S. Duan (2007), A kind of initial errors related to "spring predictability barrier" for El Niño events in Zebiak-Cane model, *Geophys. Res. Lett.*, *34*, L03709, doi:10.1029/2006GL027412.

Reynolds, R. W., and T. M. Smith (1994), Improved global sea surface temperature analyses, *J. Clim.*, *7*, 929–948, doi:10.1175/1520-0442(1994)007<0929:IGSSTA>2.0.CO;2.

Sun, L., M. Mu, D. J. Sun, and X. Y. Yin (2005), Passive mechanism of decadal variation of thermohaline circulation, *J. Geophys. Res.*, *110*, C07025, doi:10.1029/2005JC002897.

Tang, Y., and Z. Deng (2011), Bred vector and ENSO predictability in a hybrid coupled model during the period 1881–2000, *J. Clim.*, *24*, 298–314, doi:10.1175/2010JCLI3491.1.

Tang, Y., R. Kleeman, and S. Miller (2006), ENSO predictability of a fully coupled GCM model using singular vector analysis, *J. Clim.*, *19*, 3361–3377, doi:10.1175/JCLI3771.1.

Tang, Y., Z. Deng, X. Zhou, Y. Cheng, and D. Chen (2008), Interdecadal variation of ENSO predictability in multiple models, *J. Clim.*, *21*, 4811–4833, doi:10.1175/2008JCLI2193.1.

Terwisscha van Scheltinga, A. D., and H. A. Dijkstra (2008), Conditional nonlinear optimal perturbations of the double-gyre ocean circulation, *Nonlinear Processes Geophys.*, *15*, 727–734, doi:10.5194/npg-15-727-2008.

Wang, C., and J. Picaut (2004), Understanding ENSO physics—A review, in *Earth Climate: The Ocean-Atmosphere Interaction*, *Geophys. Monogr. Ser.*, vol. 147, edited by C. Wang, S.-P. Xie, and J. A. Carton, pp. 21–48, AGU, Washington, D. C.

Wu, X. G., and M. Mu (2009), Impact of horizontal diffusion on the nonlinear stability of thermohaline circulation in a modified box model, *J. Phys. Oceanogr.*, *39*, 798–805, doi:10.1175/2008JPO3910.1.

Xue, Y., M. A. Cane, and S. E. Zebiak (1997a), Predictability of a coupled model of ENSO using singular vector analysis, part I: Optimal growth in seasonal background and ENSO cycles, *Mon. Weather Rev.*, *125*, 2043–2056, doi:10.1175/1520-0493(1997)125<2043:POACMO>2.0.CO;2.

Xue, Y., M. A. Cane, and S. E. Zebiak (1997b), Predictability of a coupled model of ENSO using singular vector analysis, part II: Optimal growth and forecast skill, *Mon. Weather Rev.*, *125*, 2057–2073, doi:10.1175/1520-0493(1997)125<2057:POACMO>2.0.CO;2.

Yu, Y., W. S. Duan, and M. Mu (2009), Dynamics of nonlinear error growth and season-dependent predictability of El Niño events in the Zebiak-Cane model, *Q. J. R. Meteorol. Soc.*, *135*, 2146–2160, doi:10.1002/qj.526.

Zebiak, S. E., and A. Cane (1987), A model El Niño–Southern Oscillation, *Mon. Weather Rev.*, *115*, 2262–2278, doi:10.1175/1520-0493(1987)115<2262:AMENO>2.0.CO;2.

Zhou, X., Y. Tang, and Z. Deng (2008), The impact of nonlinear atmosphere on the fastest error growth of ENSO prediction, *Clim. Dyn.*, *30*, 519–531, doi:10.1007/s00382-007-0302-5.